metals

MDPI

Article

Non-Contact Evaluation of Deformation Characteristics on Automotive Steel Sheets

Ľubomír Ambriško [1,*] and Ladislav Pešek [2]

[1] Faculty of Mining, Ecology, Process Control and Geotechnologies, Technical University of Košice, Park Komenského 14, 042 00 Košice, Slovakia
[2] Faculty of Materials, Metallurgy and Recycling, Technical University of Košice, Park Komenského 11, 042 00 Košice, Slovakia; ladislav.pesek@tuke.sk
* Correspondence: lubomir.ambrisko@tuke.sk; Tel.: +421-55-602-2813

Abstract: The work is focused on experimental research of deformation characteristics on three grades of hot-dip galvanized steels for the automotive industry. Deformation maps were obtained using the DIC (Digital Image Correlation) method. The map documents the development of longitudinal and transverse deformations under tensile stress. In addition to uniaxial tension, the investigated specimens were subjected to eccentric tension. The stable crack growth (SCG) was evaluated using a non-contact measurement technique on CT (compact tension) specimens. The deformation of steels, which affects the resistance to stable crack growth (confirmed by the Design of Experiments—DOE method), was manifested in the first stages of eccentric loading of specimens. The notch root radius varies considerably due to the blunting of the starting fatigue crack. The resistance to stable crack growth, which represents a safety reserve during a vehicle crash, was obtained.

Keywords: deformation; DIC; stable crack growth; automotive steels; DOE

1. Introduction

Due to the rapid development of computer technology, non-contact camera methods are commonly used to detect and measure deformation.

The non-contact methods:

- allow monitoring the course of the entire test,
- allow for measuring more significant deformations,
- provide information not only about one measured length but about the whole measured area,
- they can also be used during tests at elevated temperatures.

Non-contact deformation measurement methods include (i) video-based extensometry, (ii) DIC (Digital Image Correlation), and (iii) electronic speckle pattern interferometry.

Non-contact measurement methods are very promising tools for the experimental investigation of the strain behaviors of loaded materials and structures. DIC was used in the works [1–4] to determine the fracture parameters. This method uses a mathematical correlation procedure [5] that allows the calculation of point displacements from individual, sequentially scanned, and consecutive digital images of the deformed surface. DIC is an algorithm used to process stored digital images [6]. A random pattern of speckle points must be applied to the surface of the test specimen. The reference and deformed images are first divided into subsets of the same size to calculate the displacements. Then, a correlation criterion is established between all subsets in the reference and deformed images to evaluate their similarity [7]. When matching, an algorithm divides the image into subsets and searches for corresponding partners in subsequent images using two-dimensional correlations [8]. In this way, the field of displacements for the scanned surface is obtained, from which the deformations are subsequently determined.

check for updates

Citation: Ambriško, Ľ.; Pešek, L. Non-Contact Evaluation of Deformation Characteristics on Automotive Steel Sheets. *Metals* **2024**, *14*, 566. https://doi.org/10.3390/met14050566

Received: 5 April 2024
Revised: 2 May 2024
Accepted: 8 May 2024
Published: 11 May 2024

Copyright: © 2024 by the authors. Licensee MDPI, Basel, Switzerland. This article is an open access article distributed under the terms and conditions of the Creative Commons Attribution (CC BY) license (https://creativecommons.org/licenses/by/4.0/).

DIC is a powerful optical and non-destructive measurement method for mapping the local deformation fields [9] and monitoring the change in strain distribution using image analysis [10,11].

The main advantage of using DIC over traditional methods is its ability to measure deformations in the entire field instead of at isolated points, as demonstrated in the work [12]. Work [13] presents the development of a 2D DIC procedure used to derive in-plane measurements that help to understand the origin and evolution of strain localization in mild steel. The 2D DIC technique was used to observe the localization of plastic deformation in ultrahigh-strength steel and the evolution of the deformation profile along the tensile axis between the appearance of necking and fracture [14]. Using 3D DIC in their work [15], they detected the formation and measured the shape of the deformation profile for the aluminum alloy body. DIC and videoextensometry results were compared on ultra-high-strength automotive steels [16].

DIC is suitable for measuring crack length during its growth [3]. As the crack grows, measuring the displacements close to the crack tip is essential. It allows measurement at different distances from the crack tip from the same set of images. The DIC approach differs from traditional methods in several characteristics: it has relatively high measurement accuracy, crack growth can be measured continuously during the loading, and the amount of information this approach provides is higher than other methods [17].

The innovative use of DIC as a non-invasive technique for observing crack propagation in lightweight concrete was presented in [10]. The fracture mechanisms, crack initiation, and propagation were analyzed by the camera, capturing detailed visualizations.

The failure of a metal body in technical practice is caused by crack nucleation and subsequent crack growth [18]. In this case, the fracture is carried out by the process of deformation and local failure at the crack front of a rapidly or slowly growing crack [19]. When stable crack growth occurs, the crack length increases continuously at a low speed. It may take a very long time—even many years—while the crack grows through the entire loaded section [18]. A crack can increase its length when the stress value is (i) rising, (ii) constant (e.g., creep), or (iii) time-varying (cyclic fatigue stress). Stable crack growth practically occurs in ductile (tough) fractures of metallic materials, except in cases of creep and fatigue [19]. Ductile fractures are accompanied by non-negligible plasticity at the crack front. The crack grows stable when the fracture can be quickly stabilized by decreasing or maintaining a constant value of the *J-integral*. Instability during ductile fracture occurs at the beginning of cleavage fracture after stable crack growth, by plastic instability (or collapse), or when the value of the stress intensity factor K or *J-integral* rapidly increases.

A curve that characterizes the resistance to the growth of a stable crack (stable crack growth)—the R-curve—is a suitable means to evaluate the initial stage of SCG [20,21]. The concept of R-curves was developed mainly for cases where the thickness of the structure (and therefore also the testing specimen) does not guarantee the fulfillment of the plane deformation condition [18]. The work [1] provides an alternative method for determining the R-value without assumptions. The method, based on the multi-camera DIC system, simultaneously measures deformations in three directions.

The R-curve is defined as a plot of crack extension resistance, R, as a function of slow-stable crack extension. It depends on body thickness and describes stable linear elastic fracture mechanics and growth. To describe the stable crack growth in conditions of elastic–plastic fracture mechanics, the R-curve is used again, but this time it is not expressed by the resistance of the material to crack growth [18]. Thus, the R-curve represents the dependence between the monotonically growing elastic–plastic parameter characterizing the stress and deformation field around the crack and the change in crack length. Among the types of R-curves used, can be included the dependence J–Δa, i.e., J_R-curve, where J is the value of the *J-integral* corresponding to the stable growth of the crack Δa (the *J-integral* represents the external load and characterizes the state of stress around the crack root, Δa is the displacement of the crack front due to the action of the external load). Alternatively, one can consider the dependence of *CTOD*–Δa, that is, the $CTOD_R$-curve, where *CTOD*

is the crack tip opening displacement corresponding to the stable growth of the crack Δa. *CTOD* is an alternative to the *J-integral* for expressing materials' fracture toughness and resistance to stable crack growth in the elastoplastic region.

The R-curves based on the *J-integral* have the advantage of applying the finite element method in load analysis and dimensioning of structures. The R-curve provides data on the toughness of the material and its behavior in the presence of a crack under conditions of quasi-static loading and stable crack growth. It allows us to analyze and describe the individual phases of crack growth. Its contribution lies in obtaining values that, under certain conditions, can be used to dimension structures and evaluate their defects' stability. The J_R-curve approach is also practical when applied to welded joints. The J_R-curve was initially developed as an extrapolative method to determine the J-integral's critical value in the stable crack initiation region [22]. The J_R-curve is a material property and an indicator of the material's toughness [23]. The use of the J_R-curve for stable crack growth is expected, although it is accepted that the J_R-curve may depend on the body's geometry [24]. The scope of validity, i.e., the independence of the geometry, is much more significant for the $CTOD_R$-curve [25]. The R-curve is an effective and sensitive material characteristic that can provide significant information about the properties and behavior of the material at each temperature interval [22]. The crack growth in the compact tension specimen is solved using the J_R-curve under plane stress in work [26] and the $CTOD_R$-curve in work [27].

The fracture resistance depends on the specimen geometry and load type [28]. Work [29] examined the fracture behavior covered by cyclic and static loads and a wide range of crack growth rates. Crack growth has an important role in the fracture of ceramics and glasses—crack propagation in sapphire in [30] was measured continuously under stable crack growth.

This work aims to research the deformation behavior of automotive steel sheets, including stable crack growth, which is significant in the case of ductile fractures. Both longitudinal and transverse plastic deformations of tensile specimens of three different steels were measured. A Digital Image Correlation method measured the stable crack growth of eccentric tensile specimens. The results of the experiments were set up to verify the effect on the tearing modulus using the Design of Experiments method, with three influencing factors of load, orientation, and tensile properties as variables. The effects of those factors on the tearing modulus were analyzed statistically, and finally, a prediction model was proposed.

2. Materials and Methods

Tensile tests and crack growth monitoring were performed on three experimental materials, and the non-contact method was used in the experiments. Two types of specimens were used for the experimental program: (i) standard specimens for tensile testing and (ii) specimens for eccentric tension, usually used for fracture mechanics tests. The specimens were extracted from the sheets in two orientations: parallel to the rolling direction (RD) and perpendicular to RD. For specimens (Figure 1), it means:

- specimen orientation LT—loading is parallel to the rolling direction; cracks will propagate perpendicular to RD;
- specimen orientation TL—loading is perpendicular to the rolling direction, and the crack will propagate parallel to RD.

The tensile specimens were loaded up to fracture to investigate strain field development, and the necessary data for strain calculation were taken from scanned images. On the pre-cracked specimens, notch root buckling and the initiation and propagation of SCG were observed. Both processes—strain field development and crack behavior—were monitored using the DIC technique.

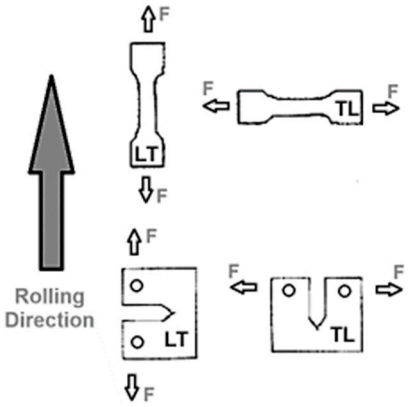

Figure 1. Tensile and CT specimens orientation (F—force).

2.1. Materials

Hot-dip, galvanized steel sheets for car bodies were used for the experiments: (i) interstitial free steel (XSG), (ii) micro-alloyed steel (HR 45), and (iii) dual-phase steel (DP). XSG and HR 45 samples were taken from deep-drawn, laser-welded, tailored blanks. The mechanical properties [31] obtained in the rolling direction (specimen orientation L) of the investigated steels are shown in Table 1. The cross-head rate in the tensile test was 0.0217 mm.s^{-1}. The thickness of the investigated steel sheets, as well as the thickness of the Zn coating, are shown in Table 1. An eXacto FN type 180-0201 device (ElektroPhysik, Köln, Germany) was used for measuring the Zn coating thickness.

Table 1. Mechanical properties of the steels examined in the rolling direction ($R_{p0.2}$—offset yield, R_e—yield strength, R_m—ultimate tensile strength, A_{80}—elongation for 80 mm gauge length, r—normal anisotropy coefficient, n—strain hardening exponent), sheet thickness B, and zinc coating thickness B_{zc}.

Steel	$R_{p0.2}$ [MPa]	R_m [MPa]	A_{80} [%]	r	n	B [mm]	B_{zc} [µm]
XSG	177	286	47.2	1.19	0.21	1.95	9.5
HR 45	360 *	449	27	0.87	0.14	1.80	12.3
DP	380	576	26.2	1	0.16	1.60	9.6

* R_e.

The Description of the Materials

XSG is a deep-drawing IF (interstitial free) steel with a ferritic microstructure (Figure 2a) and a mean grain size of 22 µm. HR 45 is a micro-alloyed steel with a ferritic–pearlitic microstructure (Figure 2b; pearlite content: 17%) with a mean grain size of 8 µm. DP is a dual-phase steel with a ferritic–martensitic microstructure (Figure 2c; martensite content: 16%) and a mean grain size of 7 µm.

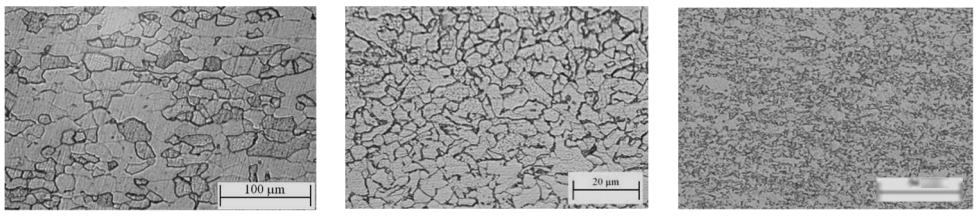

(**a**) (**b**) (**c**)

Figure 2. Microstructure of steels: (**a**) XSG, (**b**) HR 45, and (**c**) DP.

2.2. Stable Crack Growth

The non-contact displacement measurement—a videoextensometry technique—was used to monitor the stable crack growth. Guide plates ensure loading in the plane and

prevent specimen buckling during the test. Guide plates were necessary to improve optical conditions for detecting crack growth with a CCD (Charge-Coupled Device) camera on compact tension specimens. The resistance to stable crack growth was determined using J_R curves. The methodology is described in detail in the work [32].

The Instron 8511 fatigue machine (Instron, Norwood, MA, USA) was used for pre-cracking the CT specimens (width W = 50 mm) with a mechanically prepared notch (root radius = 0.4 mm). Table 2 presents the pre-cracking conditions: maximum and minimum cyclic load F_{fm}, F_{fmin}, load amplitude F_a, number of pre-cracking cycles N, and coefficient of load cycle asymmetry r_c.

Table 2. Pre-cracking conditions.

Steel	F_{fm} [N]	F_{fmin} [N]	F_a [N]	N [103]	r_c
XSG	1920	480	720	60	0.25
HR 45	3833	958	1437	30	0.25
DP	3132	783	1175	33	0.25

The loading frequency f = 45 Hz [33] was used for all steels.

The maximum loading force F_{fm} was determined according to the formula [33]:

$$F_{fm} = \frac{1}{2}\left(0.75R_y\frac{B(W-a)^2}{2W+a}\right) \quad (1)$$

where R_y is yield strength ($R_{p0.2}$ or R_e), B is the thickness of the specimen, W is the width of the specimen, and a is crack length.

2.3. DIC

Strain measurements were made on one face of a tensile specimen. The flat test bars were loaded under tension on a 200 kN Zwick testing machine (ZwickRoell, Ulm, Germany) at a cross-head rate of 0.0217 mm.s^{-1}. A speckle pattern was created on the surface of the specimen before the test. During the test, the specimen was scanned with a camera. The non-contact 3D measuring system ARAMIS (v6.1), which works on the DIC principle and uses two synchronized CCD cameras, was applied to determine the deformation characteristics under uniaxial loading. The system analyzes, recalculates, and documents deformations. It recognizes the surface of the test sample in the digital image from the camera and assigns coordinates to the pixels of the image. ARAMIS is also suitable for 3D deformation measurement under static or dynamic loading to analyze surface deformation and displacements on real structural elements [34].

The ARAMIS system follows the deformations of the test specimen in the images using many square or rectangular facets (standard facet setting according to the manufacturer: 15 × 15 px with a distance of 13 px). Each valid facet forms one measurement point. The set parameters of the facets are essential for calculating and representing the extension. The measurement result is a color map of the strain distribution on the so-called strain map. Deformations were determined for a standard facet size of 15 × 15 px.

3. Results and Discussion

The CT specimen has a notch ending in a fatigue crack. Under loading, the blunting of the crack root appears, and the crack root radius ρ changes. The crack root radius was measured from recorded images of the steel examined. The most significant root radius just before initiation of SCG was found for XSG steel, i.e., steel with the highest elongation. The steel with the lowest elongation, DP steel, shows the smallest root radius. The width before the test in Table 3 is the width of the fatigue crack. The root radius ρ is, therefore, half of that.

Table 3. Parameters of the crack root.

Steel	Width before the Test [μm]	ρ before the Test [μm]	ρ before SCG [μm]
XSG	1.3–2.6	0.65–1.3	780
HR 45	1.3–2.6	0.65–1.3	490
DP	1.3–2.6	0.65–1.3	300

The individual stages of stable crack growth are schematically documented in Figure 3. The details of the fatigue crack opening are shown in Figure 4 (a—unloaded state; the present fatigue crack is invisible) for XSG steel. In the first stage of the test, the sharp fatigue crack is blunted (Figure 4b). Initially, only elastic deformation occurs, corresponding to *J-integral* and *CTOD* values close to zero. Furthermore, the blunting occurs in the elastoplastic region (Figure 4b–i). As a result of blunting in the second stage, shear deformation of the root-stretch zone is observed [35] (Figure 4j). In the third stage, crack initiation occurs (Figure 4k), which in the fourth stage increases its length through stable growth.

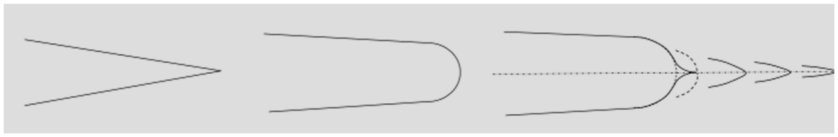

(**a**) (**b**) (**c**)

Figure 3. Schematic stable crack growth: (**a**) fatigue crack, (**b**) blunting of the crack root, and (**c**) initiation of the SCG.

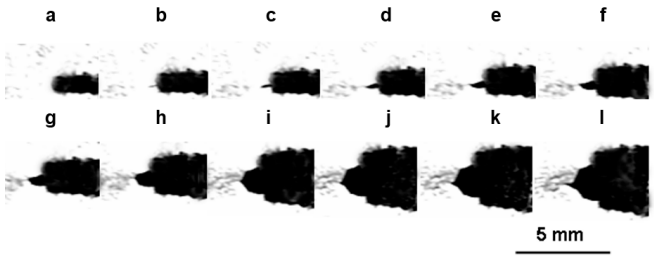

Figure 4. Opening the root of the fatigue crack (visible from (**b**)), the load increases toward the right, XSG steel ((**a**)—unloaded state, (**c–j**)—blunting of the fatigue crack root, (**k**)—crack initiation, (**l**)—stable crack growth).

The resistance to stable crack growth is expressed by the tearing modulus T [23]:

$$T = \frac{dJ}{da}\frac{E}{R_{em}^2} \qquad R_{em} = \frac{R_e + R_m}{2} \tag{2}$$

where dJ/da is the J_R-curve slope, E is Young's modulus, R_e is yield strength, and R_m is tensile strength.

XSG steel has the highest resistance, and HR 45 steel has the lowest resistance to SCG, as follows:

- XSG: T = 538
- DP: T = 124
- HR 45: T = 102.

The given T values are valid for the specimen orientation TL (Figure 1) and loading rate 0.0217 mm.s^{-1}. The work presents other determined variants [32].

The experimental results confirm that deformability impacts the resistance to stable crack growth.

Strain maps obtained just before tearing, under tensile loading on tensile testing specimens, for longitudinal and transverse deformation are shown in Figures 5–7 for all investigated steels—mapped areas showing specific deformation values, which were averaged. The specific values, determined on the same large surface, are shown in Table 4. They reach values different from elongation values for an 80 mm gauge length (Table 1). The localization of the deformation at the moment just before the tearing shows the highest value in the case of XSG steel (Table 4). Compared to tested steels, the XSG steel has the highest mean and maximum strain values expressed by both transverse and longitudinal deformation.

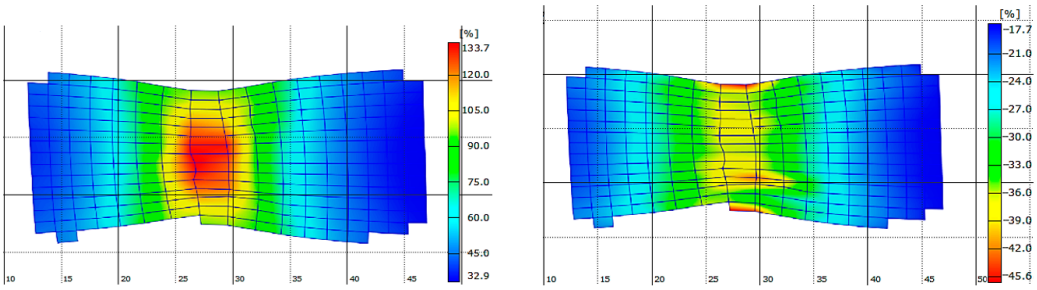

(**a**) (**b**)

Figure 5. Strain maps: (**a**) longitudinal, (**b**) transverse deformations, XSG steel.

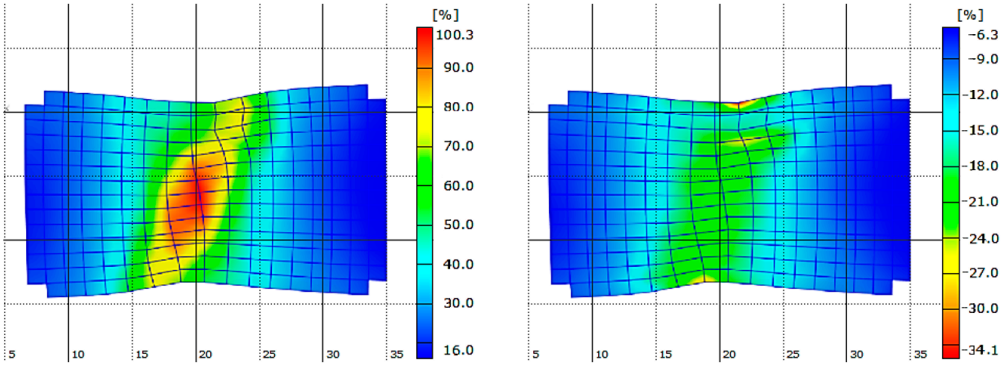

(**a**) (**b**)

Figure 6. Strain maps: (**a**) longitudinal, (**b**) transverse deformations; HR 45 steel.

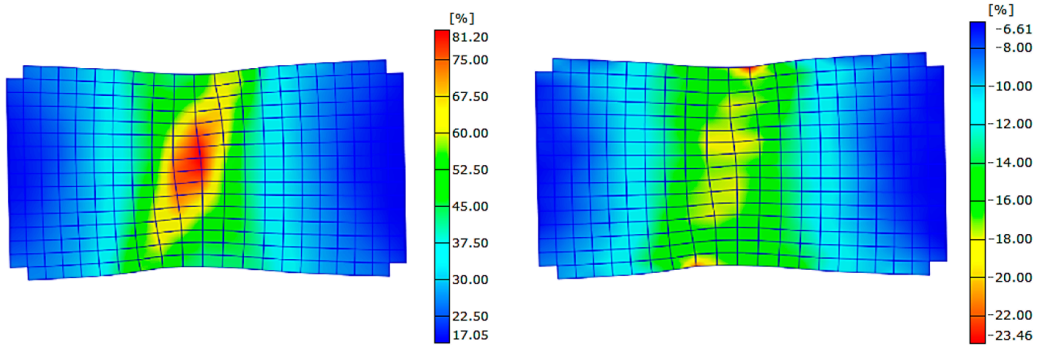

(**a**) (**b**)

Figure 7. Strain maps: (**a**) longitudinal, (**b**) transverse deformations, DP steel.

Table 4. Longitudinal (L) and transverse (T) deformation just before tearing.

Steel	L Deformation		T Deformation	
	Max. [%]	Mean [%]	Max. [%]	Mean [%]
XSG	133.7	62.9	45.7	26.5
HR 45	100.4	37.4	34.2	20.1
DP	81.2	33.8	23.5	14.5

The same area (16 × 28 mm) for all specimens was taken to evaluate strain field development and calculate strain maps for the moment just before tearing.

Suppose steel (XSG) has the lowest strength but the highest elongation, which gives this steel maximum resistance to stable crack growth. Minimum longitudinal and transverse deformation values were confirmed for DP steel, even when comparing mean or maximum values. Tensile properties do not correspond to the resistance of steels to SCG. Although DP steel has a maximum tensile strength, its elongation is the lowest and does not correspond to a minimum resistance. This suggests that resistance combines strength and elongation for higher-strength steels. Based on these findings, the Design of Experiments method [36] was used to determine the significance of the individual influences of factors and their interactions on the tearing modulus.

Experimental results from CT specimens on three types of steel, two specimen orientations, and two loading rates were the basis for two experiments designed to find possible influencing factors. Data (Table 5) were used to create an assumed model, which is an equation designed to describe the functional dependence of the output characteristic (tearing modulus) on the input factors (loading speed of the specimen, direction of sampling, and mechanical properties of steels examined). Setting the factors to a specific value is called the factor level. Two levels are often used when planning an experiment: low and high. After planning and carrying out the experiment, individual factors' influence (effect) on the response was determined. The effect of a factor is defined as the change in response caused by a change in the level of the factor. The influence of the factor can be estimated as the difference in the mean values of the response at both high and low levels of the factor [33]. Another type of influence is interaction, i.e., influence for which the influence of one factor on the response depends on one or more other factors.

Table 5. Designs of experiments with input and output values.

Run	Loading Rate [mm.s^{-1}]	Specimen Orientation [–]	Elongation [%] or R_{em} [MPa]	T [–]	Steel
1	0.0217	TL	26.2 or 478	124	DP
2	2.17	TL	26.2 or 478	129	DP
3	0.0217	LT	26.2 or 478	134	DP
4	2.17	LT	26.2 or 478	137	DP
5	0.0217	TL	47.2 or 231.5	528	XSG
6	2.17	TL	47.2 or 231.5	550	XSG
7	0.0217	LT	47.2 or 231.5	538	XSG
8	2.17	LT	47.2 or 231.5	560	XSG

In the proposed experiments, the influence of three factors was monitored (Table 6): loading rate (factor A), rolling direction (factor B), and elongation in the first draft (Experiment 1). For Experiment 2, factor C is the mean value R_{em} of yield strength R_e and ultimate tensile strength R_m (Equation (2)).

Table 6. List of input factors and their levels.

	Factors for Experiment 1	Low Level	High Level
A	Loading rate [mm.s^{-1}]	0.0217	2.17
B	Specimen orientation [–]	TL	LT
C	Elongation A_{80} [%]	26.2	47.2
	Factors for Experiment 2	**Low level**	**High level**
A	Loading rate [mm.s^{-1}]	0.0217	2.17
B	Specimen orientation [–]	TL	LT
C	R_{em} [MPa]	231.5	478

HR45 steel was not included in the experiment's design, as its tensile properties are between the lower and upper limits of monitored factors. When the crack grows parallel to the RD (specimen TL direction), the response values are smaller than when the crack grows perpendicular to the RD (specimen LT direction).

The goal was to determine which factors, or their two-factor interactions (first-order interactions), significantly affect the response, i.e., tearing modulus. A graphic display of the experiments using a cube is shown in Figure 8, while the cube corners contain the response values for individual combinations of factors. In the white-framed rectangle near the cube corner is the responding T modulus value obtained for two levels of loading rate, three types of steel, and two orientations to RD.

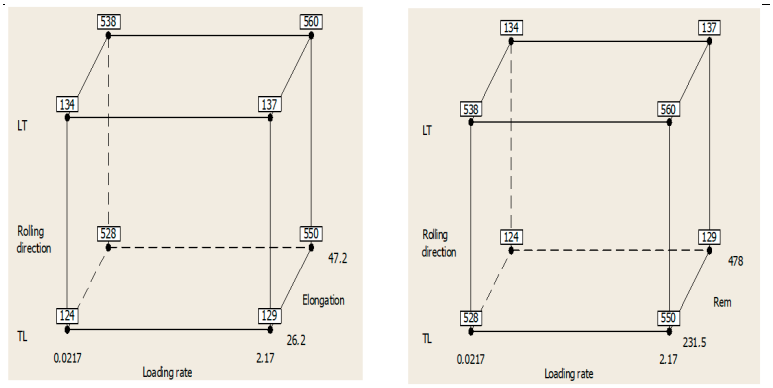

(**a**) (**b**)

Figure 8. Graphic display of the designs using a cube: (**a**) Experiment 1, (**b**) Experiment 2.

From the analysis of the effects of factors, it follows that the maximum resistance to SCG, represented by T, is achieved if we set all three factors at a high level. Table 7 shows that factor C (elongation) significantly influences the tearing modulus T. The slightest influence is factor B—orientation to RD. The significance of individual effects of factors and first-order interactions is tested using the t-test to determine the p-value.

Table 7. The main effects of factors (see also Table 6) on the response.

Experiment 1	**A Loading Rate**	**B Specimen Orientation**	**C Elongation A_{80}**
−1 (low level)	331	333	131
+1 (high level)	344	342	544
Effect of factors	13.0	9.50	413
Experiment 2	**A Loading rate**	**B Specimen Orientation**	**C R_{em}**
−1 (low level)	331	333	544
+1 (high level)	447	445	234
Effect of factors	116	113	−310

The Pareto chart (Figure 9) and the normal probability chart (Figure 10) are often used to graphically assess the significance of effects and their interactions. The Pareto chart shows the factors and interactions that statistically affect the tearing modulus at the $\alpha = 0.05$ significance level. The Pareto analysis shows that all three factors and the two-factor interaction of A and C factors statistically affect the response.

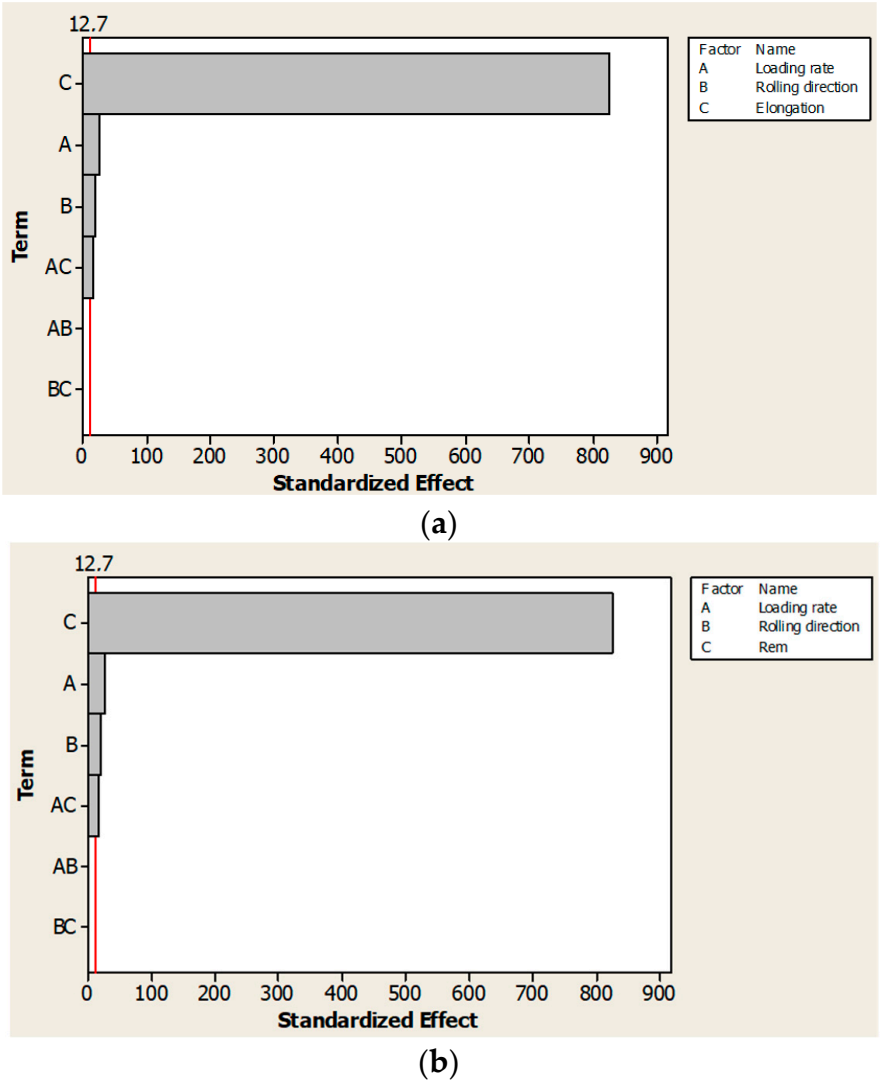

Figure 9. Pareto analysis of the significance of factors and interactions: (**a**) Experiment 1, (**b**) Experiment 2.

Factors and interactions without influence lie close to the plotted straight line (Figure 10). Factors and interactions that lie outside the plotted line are considered significant. Figures 9 and 10 show that elongation and R_{em} (factor C), loading rate (factor A), specimen orientation to RD (factor B), and interaction AC have a statistically significant influence on the response.

The interaction plots can determine Interactions between individual factors (Figure 11). If the lines shown are parallel, the interaction between the factors does not exist or is insignificant. The larger the angle of the given line segments, the greater the interaction between the monitored factors. There is no significant interaction between factors A and B and B and C. There is a significant interaction between factors A and C.

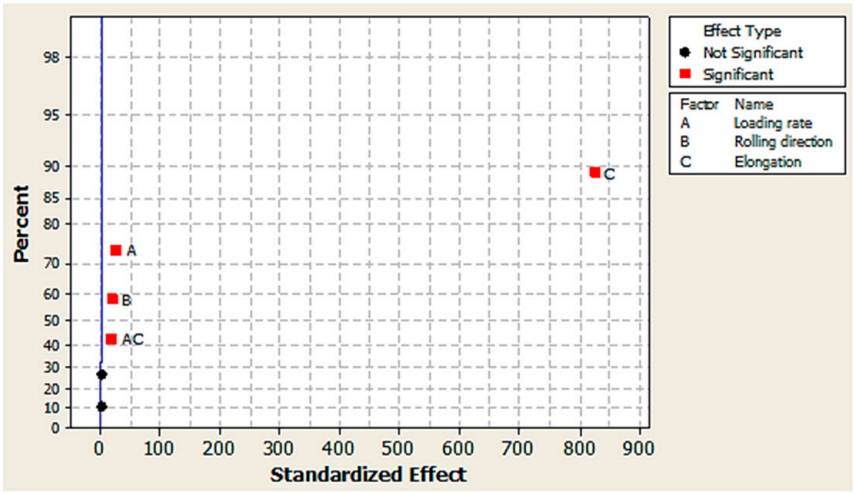

(**a**)

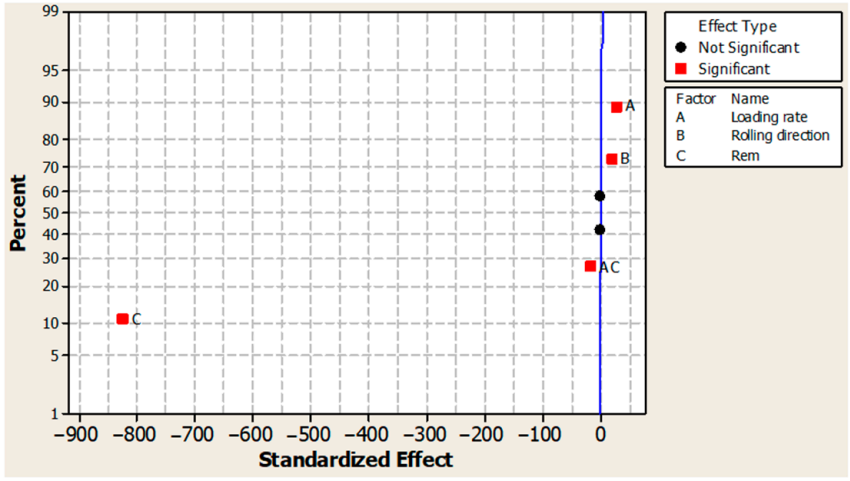

(**b**)

Figure 10. Normal probability plot of the significance of factors and interactions: (**a**) Experiment 1, (**b**) Experiment 2.

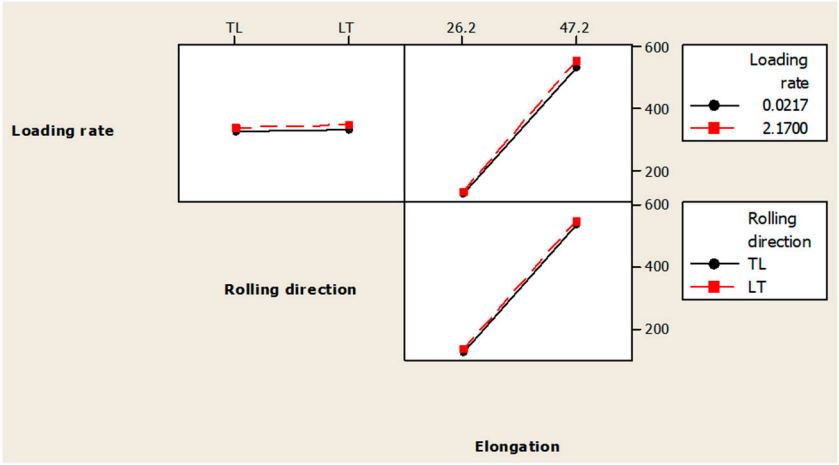

(**a**)

Figure 11. *Cont.*

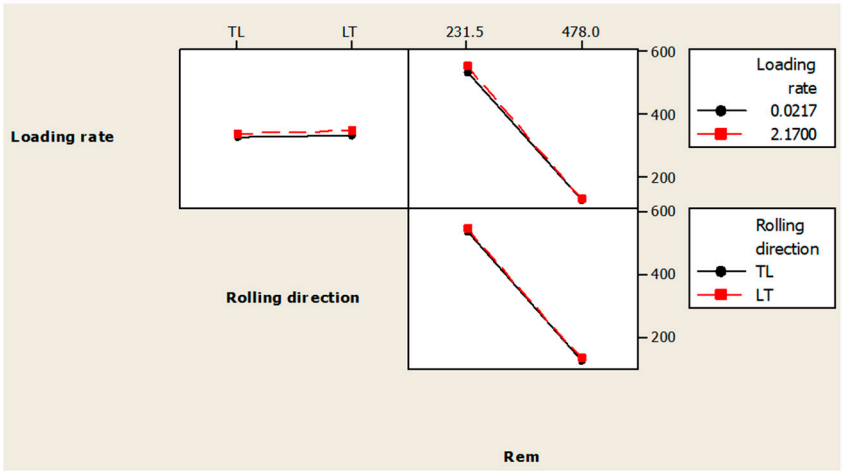

(**b**)

Figure 11. Interaction plot: (**a**) Experiment 1, (**b**) Experiment 2.

The model of the entire three-factor experiment, which contains the primary factors and all two-factor interactions, is given by the formula [36]:

$$y = \beta_0 + \beta_1 x_1 + \beta_2 x_2 + \beta_3 x_3 + \beta_{12} x_1 x_2 + \beta_{13} x_1 x_3 + \beta_{23} x_2 x_3 \quad (3)$$

where y is the T modulus (response), x_1 to x_3 represent factor values, interactions between the respective two factors (e.g., $x_1 x_2$ represents AB interaction), and β_0, β_1 to β_{23} are estimates of regression model coefficients that can also be calculated using effects. The values of all model coefficients are shown in Table 8. The values of the determination coefficient indicate that the identified regression models confirm the experimental results at 99.9%.

Table 8. Point estimation of the regression coefficients of the model.

Experiment 1	**Coefficient**	β_0	β_1	β_2	β_3	β_{12}	β_{13}	β_{23}
	Value	337.50	6.50	4.75	206.50	−0.25	4.50	0.25
	p-value	0.000	0.024	0.033	0.001	0.500	0.035	0.500
Experiment 2	**Coefficient**	β_0	β_1	β_2	β_3	β_{12}	β_{13}	β_{23}
	Value	337.50	6.50	4.8	−206.5	−0.20	−4.50	−0.20
	p-value	0.000	0.024	0.033	0.001	0.500	0.035	0.500

4. Conclusions

The stable crack growth examined in this study was determined using the non-contact method on three types of thin steel sheets. This method is suitable for its evaluation based on the R-curve by determining the tearing modulus. The resistance to stable crack growth, expressed by the tearing modulus, is the highest for interstitial-free steel. This steel showed the highest ductility and minimum strength of the steel examined. The minimum resistance was confirmed for micro-alloyed steel.

Factors affecting the stable crack growth were subjected to the application of the Design of Experiments method. The influence of loading rate, rolling direction, and ductility was monitored in the first design of the experiment. Monitoring the influence of the loading rate rolling direction and R_{em} values run through the second design. The R_{em} characterizes the area in which plastic deformation takes place. Dual-phase steel has the highest value of R_{em}; the lowest was found for interstitial-free steel. A statistically significant effect on the tearing modulus of the monitored factors was confirmed for the tensile properties. The

loading rate and orientation to the rolling direction affect the tensile properties. Thus, in the end, their influence will be reflected in the stable crack growth resistance of steels.

Author Contributions: Conceptualisation, Ľ.A.; methodology, Ľ.A. and L.P.; software, Ľ.A.; validation, Ľ.A. and L.P.; formal analysis, Ľ.A.; investigation, Ľ.A.; resources, Ľ.A.; data curation, Ľ.A.; writing—original draft preparation, Ľ.A.; writing—review and editing, Ľ.A. and L.P.; visualization, Ľ.A.; supervision, L.P.; project administration, Ľ.A.; funding acquisition, Ľ.A. All authors have read and agreed to the published version of the manuscript.

Funding: This research received no external funding.

Data Availability Statement: The raw data supporting the conclusions of this article will be made available by the authors on request.

Conflicts of Interest: The authors declare no conflicts of interest.

References

1. Fang, S.; Zheng, X.; Zheng, G.; Zhang, B.; Guo, B.; Yang, L. A new and direct R-value measurement method of sheet metal based on multi-camera DIC System. *Metals* **2021**, *11*, 1401. [CrossRef]
2. Fang, X.-Y.; Gong, J.-E.; Huang, W.; Wu, J.-H.; Ding, J.-J. Novel characterisations of effective SIFs and fatigue crack propagation rate of welded rail steel using DIC. *Metals* **2023**, *13*, 227. [CrossRef]
3. Parmadi, B.J.; Handika, N.; Sutanto, D.; Sentosa, B.O. Recycled aggregate concrete beam: Experimental study using Digital Image Correlation (DIC) and numerical study using multi-fibre Timoshenko beam element in CAST3M. In *AIP Conference Proceedings*; AIP Publishing: Damansara, Malaysia, 2023; Volume 2847.
4. Ernawan, E.; Sjah, J.; Handika, N.; Astutiningsih, S.; Vincens, E. Mechanical properties of concrete containing ferronickel slag as fine aggregate substitute using Digital Image Correlation analysis. *Buildings* **2023**, *13*, 1463. [CrossRef]
5. Bornert, M.; Brémand, F.; Doumalin, P.; Dupré, J.-C.; Fazzini, M.; Grédiac, M.; Hild, F.; Mistou, S.; Molimard, J.; Orteu, J.-J.; et al. Assessment of Digital Image Correlation measurement errors: Methodology and results. *Exp. Mech.* **2009**, *49*, 353–370. [CrossRef]
6. Kharrat, F.; Khlif, M.; Hilliou, L.; Nouri, H.; Covas, J.A.; Bradai, C.; Haboussi, M. The application of 3D-Digital Image Correlation and analytical approaches on the bulge test for biaxial characterisation of biocomposite films. *J. Braz. Soc. Mech. Sci. Eng.* **2023**, *45*, 306. [CrossRef]
7. Yang, R.; Li, Y.; Zeng, D.; Guo, P. Deep DIC: Deep learning-based Digital Image Correlation for end-to-end displacement and strain measurement. *J. Mater. Proces. Tech.* **2022**, *302*, 117474. [CrossRef]
8. DIC. Available online: http://www.limess.com (accessed on 22 August 2022).
9. Glushko, O. A simple and effective way to evaluate the accuracy of Digital Image Correlation combined with scanning electron microscopy (SEM-DIC). *Results Mater.* **2022**, *14*, 100276. [CrossRef]
10. Musalamah, S.; Purnomo, H.; Handika, N. Method for determining fracture energy of a polypropylene coarse lightweight aggregate concrete beam using Digital Image Correlation. *Eng. Proc.* **2024**, *63*, 19. [CrossRef]
11. Su, Y.; Rui, S.-S.; Han, Q.-N.; Shang, Z.-H.; Niu, L.-S.; Li, H.; Ishikawa, H.; Shi, H.-J. Estimation method of relative slip in fretting fatigue contact by Digital Image Correlation. *Metals* **2022**, *12*, 1124. [CrossRef]
12. Del Rey Castillo, E.; Allen, T.; Henry, R.; Griffith, M.; Ingham, J. Digital Image Correlation (DIC) for measurement of strains and displacements in coarse, low volume-fraction FRP composites used in civil infrastructure. *Compos. Struct.* **2019**, *212*, 43–57. [CrossRef]
13. Watrisse, B.; Chrysochoos, A.; Muracciole, J.-M.; Némoz-Gaillard, M. Analysis of strain localisation during tensile tests by Digital Image Correlation. *Exp. Mech.* **2001**, *41*, 29–39. [CrossRef]
14. Eman, J.; Sundin, K.G.; Oldenburg, M. Spatially resolved observations of strain fields at necking and fracture of anisotropic hardened steel sheet material. *Int. J. Solids Struct.* **2009**, *46*, 2750–2756. [CrossRef]
15. Dick, C.P.; Korkolis, Y.P. Mechanics and full-field deformation study of the ring hoop tension test. *Int. J. Solids Struct.* **2014**, *51*, 3042–3057. [CrossRef]
16. Hlebova, S.; Ambrisko, L.; Pesek, L. Strain measurement in local volume by non-contact videoextensometric technique on ultra high strength steels. *Key Eng. Mater.* **2014**, *586*, 129–132.
17. DIC. Available online: https://home.iitm.ac.in/kramesh/DIC.pdf (accessed on 20 August 2022).
18. Vlk, M.; Florian, Z. *Limit States and Reliabilit*, 1st ed.; VÚT: Brno, Czech Republic, 2007; pp. 29–32. (In Czech)
19. Trebuňa, F.; Šimčák, F. *Resistance of Elements of Mechanical Systems*, 1st ed.; Edícia vedeckej a odbornej literatúry TU: Košice, Slovakia, 2004; pp. 51–52. (In Slovak)
20. Ambrisko, L.; Pesek, L. Determination the crack growth resistance of automotive steel sheets. *Chem. Listy* **2011**, *105*, 767–768.
21. Ambrisko, L.; Cehlar, M.; Marasova, D. The rate of stable crack growth (SCG) in automotive steels sheets. *Metalurgija* **2017**, *56*, 396–398.
22. Trebuňa, F.; Buršák, M. *Limit States—Quarries*, 1st ed.; Edícia vedeckej a odbornej literatúry TU: Košice, Slovakia, 2002; pp. 33–34. (In Slovak)

23. Saxena, A. *Nonlinear Fracture Mechanics for Engineers*, 1st ed.; CRC Press: Boca Raton, FL, USA, 1998; pp. 154–156.
24. Dhar, S.; Marie, S.; Chapuliot, S. Determination of critical fracture energy, Gfr, from crack tip stretch. *Int. J. Press. Vessels Pip.* **2008**, *85*, 313–321. [CrossRef]
25. Brocks, W.; Anuschewski, P.; Scheider, I. Ductile tearing resistance of metal sheets. *Eng. Fail. Anal.* **2010**, *17*, 607–616. [CrossRef]
26. Kumar, S.; Singh, I.V.; Mishra, B.K. A coupled finite element and element-free Galerkin approach for the simulation of stable crack growth in ductile materials. *Theor. Appl. Fract. Mech.* **2014**, *70*, 49–58. [CrossRef]
27. Maiti, S.K.; Krishna Kishore, G.; Mourad, A.-H.I. Bilinear CTOD/CTOA scheme for characterisation of large range mode I and mixed mode stable crack growth through AISI 4340 steel. *Nucl. Eng. Des.* **2008**, *238*, 3175–3185. [CrossRef]
28. Xu, W.; Ren, Y.; Xiao, S.; Liu, B. A finite crack growth energy release rate for elastic-plastic fracture. *J. Mech. Phys. Solids* **2023**, *181*, 105447. [CrossRef]
29. Kovarik, O.; Cizek, J.; Klecka, J. Fatigue crack growth rate description of RF-plasma-sprayed refractory metals and alloys. *Materials* **2023**, *16*, 1713. [CrossRef]
30. Jiang, J.; Falco, S.; Wang, S.; Giuliani, F.; Todd, R.I. Microcantilever investigation of slow crack growth and crack healing in aluminium oxide. *Acta Mater.* **2024**, 119914, *in press*. [CrossRef]
31. Pribulova, A.; Babic, J.; Baricova, D. Influence of Hadfield's steel chemical composition on its mechanical properties. *Chem. listy* **2011**, *105*, 430–432.
32. Ambrisko, L.; Pesek, L. The crack growth resistance of thin steel sheets under eccentric tension. *Sadhana* **2018**, *43*, 25. [CrossRef]
33. *STN 42 0347*; Metal Testing, Fracture Toughness of Metals under Static Load. Slovak Technical Standard: Bratislava, Slovakia, 1990. (In Slovak)
34. GOM; ARAMIS. *User Manual—Software*; GOM: Braunschweig, Germany, 2012.
35. Ambrisko, L.; Pesek, L. The stretch zone of automotive steel sheets. *Sadhana* **2014**, *39*, 525–530. [CrossRef]
36. Montgomery, D.C. *Design and Analysis of Experiments*, 10th ed.; J. Wiley: New York, NY, USA, 2020; pp. 97–99.

Disclaimer/Publisher's Note: The statements, opinions and data contained in all publications are solely those of the individual author(s) and contributor(s) and not of MDPI and/or the editor(s). MDPI and/or the editor(s) disclaim responsibility for any injury to people or property resulting from any ideas, methods, instructions or products referred to in the content.